Inorganic Chemistry

pubs.acs.org/IC

Article

High-Pressure Synthesis and Magnetism of the 4*H*-$BaMnO_3$ Single Crystal and Its 6*H*-Type Polymorph

Shijun Qin, Yi-Ying Chin, Bowen Zhou, Zhehong Liu, Xubin Ye, Jia Guo, Guangxiu Liu, Chien-Te Chen, Zhiwei Hu, and Youwen Long*

Cite This: *Inorg. Chem.* 2021, 60, 16308−16315

Read Online

ACCESS | Metrics & More | Article Recommendations | Supporting Information

ABSTRACT: A 4*H*-type $BaMnO_3$ single crystal was prepared by combining the floating zone method with high-pressure treatment at 5 GPa and 1023 K. The crystal crystallizes to a hexagonal structure with space group $P6_3/mmc$ and lattice parameters a = 5.63723(5) Å and c = 9.22355(8) Å. In this structure, face-sharing MnO_6 octahedral dimers connect with each other by corner O atoms along the c-axis direction, forming an -A-B-A-C-type 4*H* arrangement. A long-range antiferromagnetic (AFM) phase transition is found to occur at $T_N \approx$ 263 K. When the synthesis pressure increases to 20 GPa, a new polymorphic phase is obtained. This higher-pressure phase still possesses the hexagonal $P6_3/mmc$ symmetry, but the lattice parameters change to be a = 5.61349(2) Å and c = 13.66690(9) Å with a unit cell volume reduction of 2.05%. In this new phase, the c-axis MnO_6 dimers are separated by MnO_6 octahedral layers in the ab plane, forming an -A−B-C-A-C-B-type 6*H* structure. The 6*H* phase exhibits two long-range AFM orderings at $T_{N1} \approx$ 220 K and $T_{N2} \approx$ 25 K, respectively. The different magnetic properties are discussed on the basis of the detailed structural constitutions of 4*H*- and 6*H*-$BaMnO_3$.

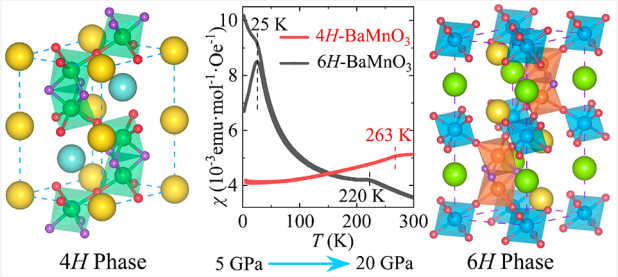

INTRODUCTION

Perovskite structure oxides with a chemical formula of ABO_3 have diverse structural derivatives and A-B charge combinations and thus exhibit a series of interesting physical properties in magnetism, electrical transport, magnetoelectric coupling, and chemical catalysis.[1−8] The detailed crystal structure of perovskite is closely related to the relative size of cations at both A and B sites. Goldschmidt's tolerance factor, $t = (r_A + r_O)/(\sqrt{2})(r_B + r_O)$, is often used to describe such a relationship.[9,10] Here r_A, r_B, and r_O denote the ionic radii of A, B, and O ions, respectively. When t = 1, an ideal cubic perovskite structure with corner-sharing rigid octahedra is expected to be present. In most cases, however, the value of t deviates from unity due to the cooperating octahedral distortions (including tilting and rotating). For a larger A-site ion such as Ba^{2+}, the related perovskite usually tends to crystallize into a hexagonal structure with t > 1. In such a structure, both face- and corner-sharing BO_6 octahedra may emerge. Different combinations of these two types of octahedra can lead to different hexagonal stacking structures.[11]

The manganese-based perovskite family of $A^{2+}Mn^{4+}O_3$ (A = Ca, Sr, Ba) displays a wide variety of structural evolutions with the variation of the A-site ionic size. At ambient pressure, $CaMnO_3$ (t = 0.989) has an orthorhombic perovskite structure which is composed only of corner-sharing MnO_6 octahedra.[12] In comparison, $SrMnO_3$ (t = 1.033) crystallizes to a 4*H*-type hexagonal structure due to the larger A-site size.[13] Moreover, 4*H*-$SrMnO_3$ is very sensitive to external pressure. It will change to a 6*H*-type hexagonal structure and a 3*C*-type cubic phase if high pressure is applied during the synthesis at 5 and 7 GPa, respectively.[14,15] Corresponding to the structural evolutions, the AFM phase-transition temperatures also change from 280 K in the 4*H* phase to 235 K in the 6*H* phase and then to 240 K in the 3*C* phase.[13,16] Compared with $SrMnO_3$, the pressure-related structural transformations of $BaMnO_3$ (t = 1.078)[17] are more complex. Different from the 4*H* phase of $SrMnO_3$, $BaMnO_3$ crystallizes to a 2*H* hexagonal structure at ambient pressure. The 2*H* phase changes toward a 9*R* hexagonal phase at 3−7.5 GPa and then to a 4*H* phase with pressure increasing to 9 GPa.[14] All of the MnO_6 octahedra are face-sharing in 2*H*-$BaMnO_3$, forming 1D-like spin chains with a shorter Mn−Mn distance (2.407 Å) along the c axis.[18] Possible polar structure and multiple magnetic phase transitions are proposed for this phase. 9*R*-$BaMnO_3$ has a different hexagonal structure with a space group of $R\bar{3}m$, and a higher-temperature AFM transition occurs at around 350 K.[14,19,20] Although the 6*H* and 3*C* phases are observed in $SrMnO_3$, the counterparts are absent in

Received: July 16, 2021
Published: October 18, 2021

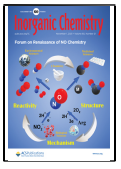

https://doi.org/10.1021/acs.inorgchem.1c02155
Inorg. Chem. 2021, 60, 16308−16315

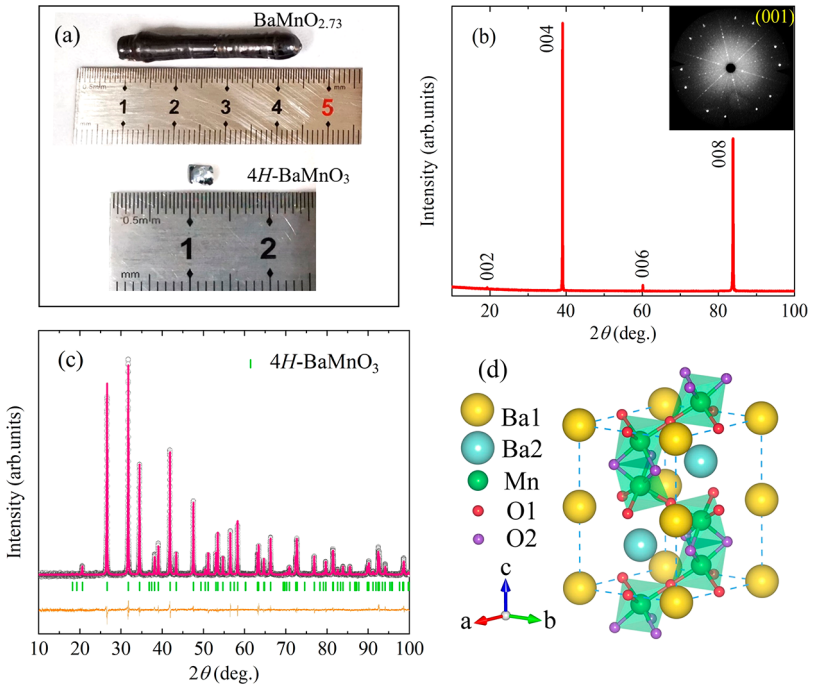

Figure 1. (a) Morphology of $BaMnO_{2.73}$ and $4H$-$BaMnO_3$ single crystals. (b) XRD pattern for the highly symmetrical (001) plane. The inset shows the Laue diffraction spots of this plane. (c) Powder XRD pattern at room temperature and Rietveld refinement results of a pulverized $4H$-$BaMnO_3$ single crystal. The observed (black circles), calculated (pink line), and difference (orange line) patterns are shown. The green ticks indicate the allowed Bragg reflections with space group $P6_3/mmc$. (d) Schematic crystal structure of $4H$-$BaMnO_3$. Face- and corner-sharing MnO_6 octahedra alternately connect along the c-axis direction and forming a chain-like distribution.

$BaMnO_3$ to date. Moreover, all of the reported high-pressure phases of $BaMnO_3$ are polycrystalline,[14,20,21] where the detailed oxygen content and intrinsic magnetism remain for further evaluation. Therefore, it is pressing to prepare $BaMnO_3$ single crystals under high pressure. In this work, we successfully prepared high-quality single crystals of $4H$-$BaMnO_3$ under high-pressure and moderate temperature conditions for the first time. When a higher pressure was applied to $4H$-$BaMnO_3$, a new $6H$ hexagonal phase was obtained. Detailed magnetic properties were studied for these two polymorphic phases.

EXPERIMENTAL DETAILS

The polycrystalline $BaMnO_{2.73}$ precursor was prepared by a solid-state reaction method.[21,22] Appropriate amounts of very pure (99.9%) $BaCO_3$ and Mn_2O_3 powders with a molar ratio of 1:2 were thoroughly mixed and then held at 1373 K for 24 h under flowing Ar gas. The resulting product was reground in air and pressed into a rod of 4.3 mm diameter at 200 MPa before being heated for 10 h at 1373 K in flowing Ar. The annealing rod was adopted to grow the oxygen-deficient $BaMnO_{2.73}$ single crystal by using the floating zone method with a growth rate of 2.8 mm/h in an Ar atmosphere. To obtain oxygen-full $4H$-$BaMnO_3$ single crystals, the oxygen-deficient precursor of the $BaMnO_{2.73}$ single-crystal rod was cut and polished into a pellet with a diameter of 4 mm and a height of 2 to 3 mm. The pellet single crystal was sealed in a gold capsule with the use of excess (3-fold) $KClO_4$ oxidizing agent.[23−25] Then, the sealed gold capsule was put into the high-pressure assembly and treated on a large volume cubic-anvil-type high-pressure apparatus at 5 GPa and 1023 K for 60 min. To prepare the $6H$ phase of $BaMnO_3$, the $4H$-type single-crystal powders were further treated at 20 GPa and 1473 K for 30 min using Walker-type two-stage high-pressure equipment. During this higher-pressure and -temperature treatment, some $KClO_4$ oxidizing agent was also adopted to ensure the oxygen stoichiometry ($4H$-$BaMnO_3$:$KClO_4$ = 3:1 by weight). In our attempts, the $6H$-$BaMnO_3$ phase cannot be obtained if a $4H$-type single-crystal bulk was used for such a treatment. In addition, we did not find any trace of the formation of the $6H$-type phase at synthesis pressures of 10 and 15 GPa.

Powder X-ray diffraction (XRD) and Laue back reflection were used to identify the crystal quality and structure using a Huber diffractometer at room temperature (RT) with Cu $K\alpha_1$ radiation. The powder diffraction range of the 2θ angle is from 10 to 100° with a step length of 0.005°. Structural refinement for the XRD data was performed on the basis of the Rietveld method using the GSAS program.[26] X-ray absorption spectroscopy (XAS) at the Mn-$L_{2,3}$ edges was measured at the BL07A NSRRC beamline using the total electron yield mode at RT. The temperature-dependent magnetic susceptibility and isothermal magnetization behavior were measured using a superconducting quantum interference device magnetometer (Quantum Design, MPMS-VSM). Specific heat data were obtained on a physical property measurement system (Quantum Design, PPMS-9T) at zero magnetic field. Bulk pieces were used for both magnetic and specific heat measurements.

RESULTS AND DISCUSSION

Figure 1a shows the single crystal of the precursor of $BaMnO_{2.73}$ grown by the floating zone method. The powder XRD of the precursor crystal shows very similar features to that of the $4H$-$BaMnO_{2.75}$ polycrystalline as reported by Parras et al.,[22] suggesting the formation of a $4H$ hexagonal structure with space group $P6_3/mmc$ and lattice constants a = 5.6739(1) and c = 9.3280(2) Å (Figure S1 and Table S1). According to the oxygen occupancy as well as the refined Mn−O distances, the oxygen content of the precursor crystal is temporarily determined to be about 2.73. After a high oxygen pressure treatment, an oxygen full $BaMnO_3$ single crystal can be obtained. Figure 1b shows a cut piece of a $BaMnO_3$ single crystal with the size of 2 × 1 × 1 mm^3, where the widest surface is the (001) plane as identified by Laue diffraction. As

https://doi.org/10.1021/acs.inorgchem.1c02155
Inorg. Chem. 2021, 60, 16308−16315

shown in the inset of Figure 1b, the sharp Laue diffraction spots of the highly symmetrical (001) plane confirm the high quality of the $BaMnO_3$ single crystals that we obtained. When the XRD diffraction was performed on this plane, only 00*h* (*h* = even numbers) peaks can be observed, suggesting that the as-made crystal has a single domain. Furthermore, the $BaMnO_3$ single crystal was crushed into powders for XRD measurement. Figure 1c presents the powder XRD pattern as well as the Rietveld refinement results. All of the diffraction peaks can be well fitted based on a 4*H*-type hexagonal perovskite structure with space group of $P6_3/mmc$.

Table 1 shows the refined structural parameters. The refined lattice constants are a = 5.63723(5) Å and c = 9.22355(8) Å,

Table 1. Refined Structure Parameters for the 4*H*-Type $BaMnO_3$ (Z = 4) and the BVS Result for Mn at Room Temperature[a]

parameter	value	parameter	value
a (Å)	5.63723(5)	Ba1−O1(Å) × 6	2.81861(2)
c (Å)	9.22355(8)	Ba1−O2(Å) × 6	2.965(3)
V (Å^3)	253.840(6)	Ba2−O1(Å) × 6	2.82229(2)
Mn_z	0.1131(1)	Ba2−O2(Å) × 6	2.828(4)
$O2_x$	0.1909(4)	Mn−O1 (Å) × 3	1.9331(6)
$O2_y$	0.3817(8)	Mn−O2 (Å) × 3	1.879(3)
Uiso(Ba1) (100 × Å^2)	0.184(2)	∠Mn−O1−Mn (deg)	180.00
Uiso(Ba2) (100 × Å^2)	0.060(2)	∠Mn−O2−Mn (deg)	84.5(2)
Uiso(Mn) (100 × Å^2)	0.035(3)	BVS (Mn)	3.96
Uiso(O1) (100 × Å^2)	0.477(2)	R_{wp} (%)	2.08
Uiso(O2) (100 × Å^2)	0.282(2)	R_p (%)	1.49

[a]Space group $P6_3/mmc$ (no. 194); atomic sites are Ba1 2*a* (0, 0, 0), Ba2 2*d* (1/3, 2/3, 1/4), Mn 4*f* (1/3, 2/3, *z*), O1 6*g* (0.5, 0, 0), and O2 6*h* (*x*, *y*, 1/4). BVS values (V_i) were calculated using the formula $V_i = \sum_j S_{ij}$, with $S_{ij} = \exp[(r_0 - r_{ij})/0.37]$ and $r_0(Mn^{4+})$ = 1.753 Å.[43]

which are slightly less than those reported for a polycrystalline sample (a = 5.6376 Å and c = 9.2241 Å),[21] indicating that the single crystal is closer to having the oxygen stoichiometry. The refined Mn−O distances vary from 1.879(3) Å to 1.9331(6) Å, suggesting a moderate octahedral distortion, as observed in the 4*H*-$SrMnO_3$.[13,16] According to the Mn−O bond lengths, the bond valence sum (BVS) calculations demonstrate the presence of a Mn^{4+} valence state (Table 1), indicating that the oxygen content should be very close to the stoichiometric value. Figure 1d presents the schematic crystal structure of the 4*H*-type $BaMnO_3$. One can find that a couple of MnO_6 octahedra form a dimer by sharing the face, and then the dimers are connected to each other through the corner-sharing oxygen atom along the c axis.

Figure 2a shows the XRD pattern as well as the Rietveld structural refinement results for $BaMnO_3$ further treated at 20 GPa. Compared with the 4*H* phase mentioned above, this product exhibits an essentially different diffraction pattern. All of the diffraction peaks of this higher-pressure phase can be fitted on the basis of a structure model similar to that of the 6*H*-$SrMnO_3$ or 6*H*-$BaCrO_3$ with a space group of $P6_3/mmc$.[16,27] Table 2 lists the refined structural parameters, which include lattice constants, atomic positions, and selected bond lengths and bond angles. The lattice constants of this new phase are a = 5.61349(2) Å and c = 13.66690(9) Å. Both are

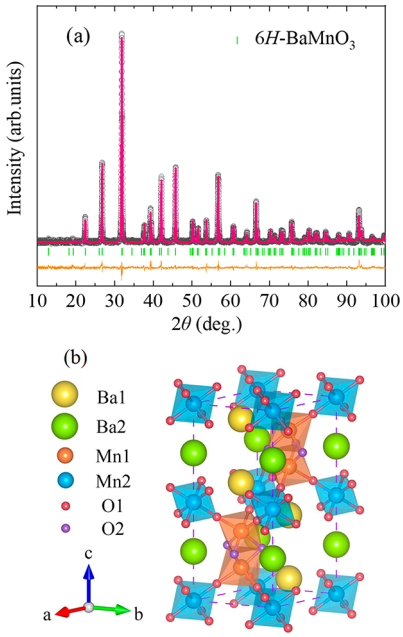

Figure 2. (a) XRD pattern at RT and Rietveld refinement results of the 6*H*-$BaMnO_3$ single crystal. The observed (black circles), calculated (pink line), and difference (orange line) patterns are shown. The green ticks indicate the allowed Bragg reflections with space group $P6_3/mmc$. (b) Schematic crystal structure of 6*H*-$BaMnO_3$, where face-sharing octahedral dimers along the c axis are separated by MnO_6 octahedral layers in the *ab* plane.

Table 2. Refined Structure Parameters for the 6*H*-Type $BaMnO_3$ (Z = 6) and the BVS Result for Mn at Room Temperature[a]

parameter	value	parameter	value
a (Å)	5.61349(2)	Uiso(O2) (100 × Å^2)	0.396(9)
c (Å)	13.66690(9)	Ba1−O1(Å) × 6	2.8091(2)
V (Å^3)	372.964(3)	Ba1−O1(Å) × 3	2.842(4)
$Ba1_z$	0.08857(6)	Ba1−O2(Å) × 3	2.864(3)
$Mn1_z$	0.6577(1)	Ba2−O1(Å) × 6	2.808(4)
$O1_x$	0.1632(4)	Ba2−O2(Å) × 6	2.8143(4)
$O1_y$	0.3265(9)	Mn1−O1 (Å) × 3	1.962(4)
$O1_z$	0.5805(3)	Mn1−O2 (Å) × 3	1.895(4)
$O2_x$	0.5212(5)	Mn2−O1 (Å) × 6	1.931(4)
$O2_y$	0.0425(1)	∠Mn1−O1−Mn2 (deg)	177.8(2)
Uiso(Ba1) (100 × Å^2)	0.142(9)	∠Mn1−O2−Mn1 (deg)	83.5(2)
Uiso(Ba2) (100 × Å^2)	0.067(9)	BVS (Mn1)	3.72
Uiso(Mn1) (100 × Å^2)	0.163(9)	BVS (Mn2)	3.68
Uiso(Mn2) (100 × Å^2)	0.535(9)	R_{wp} (%)	2.99
Uiso(O1) (100 × Å^2)	0.367(9)	R_p (%)	2.21

[a]Space group $P6_3/mmc$ (no. 194); atomic sites are Ba1 4*f* (1/3, 2/3, *z*), Ba2 2*b* (0, 0, 1/4), Mn1 4*f* (1/3, 2/3, *z*), Mn2 2*a* (0, 0, 0), O1 12*k* (*x*, *y*, *z*), and O2 6*h* (*x*, *y*, 1/4). The methods of BVS calculation are the same as mentioned in Table 1.

slightly larger than those of 6*H*-$SrMnO_3$ with a = 5.4289 Å and c = 13.4025 Å[16] due to the larger ionic radius of Ba^{2+} compared to that of Sr^{2+}.[42] When $BaMnO_3$ changes from the 4*H* to 6*H* phase under a higher pressure, the unit cell volume per

https://doi.org/10.1021/acs.inorgchem.1c02155
Inorg. Chem. 2021, 60, 16308−16315

chemical formula is reduced by 2.05%, indicating that the 6*H* phase is a higher-density phase, as expected from the higher synthesis pressure. Moreover, there exist distinct structural constructions between the 4*H* and 6*H* phases. For example, in contrast to the corner-sharing MnO_6 octahedral dimers along the *c* axis as observed in the 4*H* phase, a MnO_6 octahedral layer is formed between the dimers in the *ab* plane. The in-plane octahedra are connected to the dimers by sharing the corner O atoms. As a result, there are two distinct Mn positions (Mn1 and Mn2) in the 6*H* phase, while only a single Mn position is involved in the 4*H* phase.

According to the Mn−O bond lengths shown in Table 2, the valence of Mn was calculated by BVS to be +3.72 for Mn1 and +3.68 for Mn2, suggesting the formation of the Mn^{4+} state in the 6*H* phase. In comparison, the BVS value of Mn is reduced from +3.96 in the 4*H* phase to an average +3.70 in the 6*H* phase. Such a reduction may be attributed to the possible covalent effects caused by the pressure-enhanced p−d hybridizations duo to the much higher synthesis pressure of the 6*H* phase (20 GPa) relative to that of the 4*H* phase (5 GPa). As is well known, XAS is highly sensitive to the valence states[28−32] and local environments[33−36] for 3d transition metals. This technique was used to further determine the valence state of Mn in $BaMnO_3$. Figure 3 shows the Mn-$L_{2,3}$ edges of 4*H*- and 6*H*-$BaMnO_3$ together with the Mn^{3+} reference $LaMn^{3+}O_3$[31] and the Mn^{4+} reference $SrMn^{4+}O_3$[31] with similar MnO_6 octahedral coordination. Compared with $LaMnO_3$, the absorption peaks of both 4*H*- and 6*H*-$BaMnO_3$ shift to a higher energy by about 1.3 eV, indicating that the valence state of Mn is higher than +3 in the two phases of $BaMnO_3$. Furthermore, both of them are consistent with the absorption peak energy position and peak profile of the Mn^{4+} reference $SrMnO_3$, confirming the formation of the Mn^{4+} state as well as the oxygen stoichiometry in the 4*H* and 6*H* phases.

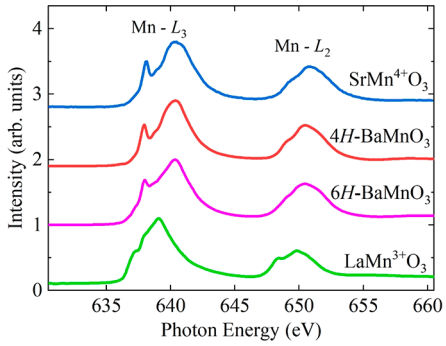

Figure 3. X-ray absorption spectra at the Mn-$L_{2,3}$ edges for 4*H*- and 6*H*-$BaMnO_3$ together with related reference compounds $SrMnO_3$ and $LaMnO_3$ for comparison.[31]

Figure 4a shows the temperature dependence of magnetic susceptibility measured at 0.1 T with the field parallel and perpendicular to the high-symmetry plane (001) on the 4*H*-$BaMnO_3$ single crystal. One finds that the perpendicular direction shows a larger magnitude in susceptibility than that of the parallel direction, reflecting the anisotropic nature of magnetism as expected from the hexagonal crystal structure. Along both directions, the susceptibility experiences an apparent decrease at a critical temperature of $T_N \approx 263$ K, suggesting the occurrence of a long-range AFM phase transition.[21] The inset of Figure 4a shows the derivative of susceptibility curves along the two directions, where sharp peaks can be observed at T_N. It is notable that, above T_N, the magnetic susceptibility curves that we measured show slight increases with increasing temperature. This feature deviates from the typical paramagnetic behavior and can be attributed to some 1D short-range AFM correlations, as reported in the hexagonal $SrMnO_3$.[16]

Corresponding to the long-range AFM phase transition observed in the 4*H*-$BaMnO_3$, a sharp λ-type anomaly is also found to occur near T_N. At lower temperatures (<15 K), the specific heat data can be fitted using the formula $C_p = \beta T^3 + \delta T^5$. (See the inset of Figure 4b, yielding the coefficient $\beta = 1.59(1) \times 10^{-4}$ J mol^{-1} K^{-4}, and $\delta = 2.96(7) \times 10^{-7}$ J mol^{-1} K^{-6}.) The result indicates that phonon and AFM excitations contribute to the specific heat.[37] Figure 4c presents the isothermal magnetization curves measured at different temperatures with the field perpendicular to the (001) plane. In accordance with the AFM feature, linear magnetization behaviors are found to occur. In addition, we also compare the magnetization with the field parallel and perpendicular to the plane. As shown in Figure 4d, both directions show similar linear magnetization behaviors, but the magnitude of the perpendicular direction is somewhat larger than that of the parallel one, in agreement with the susceptibility measurements.

Figure 5a,b reflects the magnetic properties of 6*H*-$BaMnO_3$ by susceptibility and specific heat measurements. The magnetic susceptibility curve of the 6*H* phase is significantly different from that of the 4*H* phase. As the temperature decreases, the 6*H* phase shows a kink at $T_{N1} \approx 220$ K (Figure 5a), where a sharp λ-type specific heat anomaly also appears (Figure 5b), indicating the occurrence of a long-range AFM phase transition. On further cooling to $T_{N2} \approx 25$ K, the susceptibility displays a second sharp peak with significant separation between ZFC and FC curves below this temperature. Moreover, frequency-independent peaks are also observed in ac susceptibility curves at around 25 K (Figure 5d), confirming the presence of another long-range AFM phase transition. The remarkable ZFC and FC separation may originate from the canted AFM spins.[16] Although the 4*H* phase shows some short-range 1D AFM correlations above the T_N, the 6*H* phase follows the Curie−Weiss law at temperatures above 250 K. When the $\chi^{-1} = (T - \theta)/C$ function was used to fit the inverse susceptibility data, one could obtain the Weiss temperature, $\theta = -219$ K, and the Curie constant, $C = 1.842$ emu·K/mol. The absolute value of the Weiss temperature is very close to T_{N1}, and the negative signal agrees with the AFM interactions. According to the fitted Curie constant, the effective magnetic moment is calculated to be $\mu_{eff} = 3.84\ \mu_B$/f.u., which is comparable to the theoretical value (3.87 μ_B/f.u.) for a Mn^{4+} state with $S = 3/2$ in a localized electronic model. This result also demonstrates the stoichiometric oxygen content of 6*H*-$BaMnO_3$, in agreement with the XAS measurement.

In accordance with the long-range AFM and paramagnetic properties, linear magnetization behaviors without visible hysteresis are observed above T_{N2} (e.g., at 100 and 250 K) in 6*H*-$BaMnO_3$ (Figure 5c). In contrast, there exists clear magnetic hysteresis at 2 K, which is consistent with the canted AFM spins occurring at T_{N2} as mentioned above. The coercive field observed at 2 K is about 2700 Oe. Although the 6*H* phase exhibits a sharp peak in dc magnetic susceptibility and frequency-independent peaks in ac susceptibility at around T_{N2}, the specific heat smoothly changes at this critical temperature (Figure 5b). We infer that most magnetic entropy

https://doi.org/10.1021/acs.inorgchem.1c02155
Inorg. Chem. 2021, 60, 16308−16315

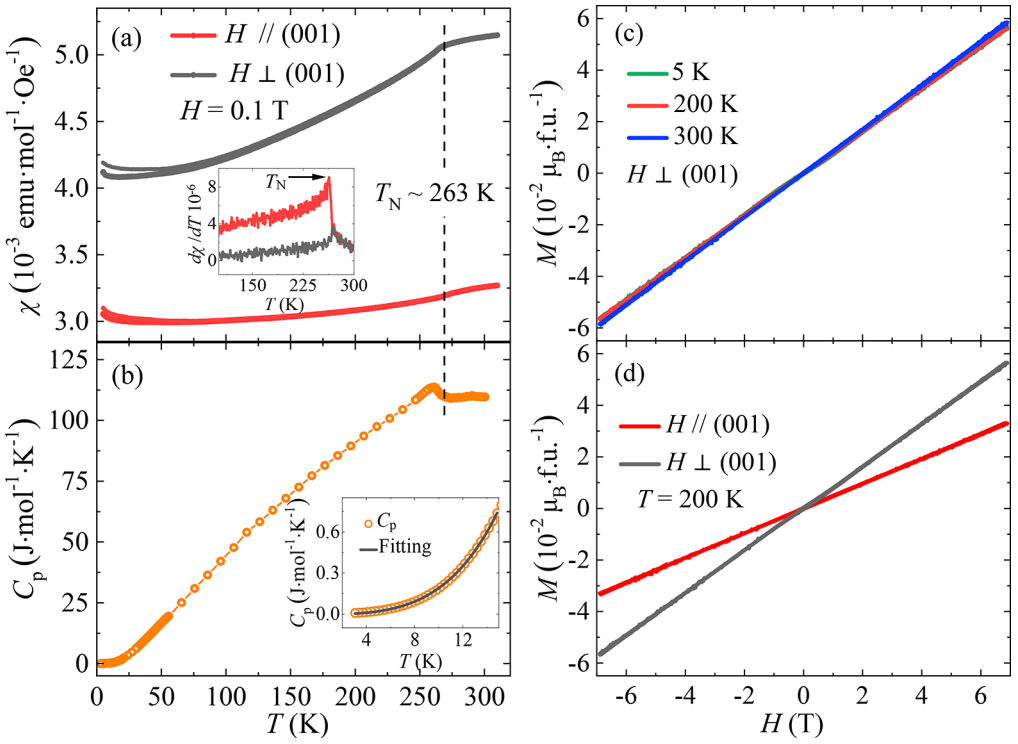

Figure 4. (a) Temperature-dependent magnetic susceptibility (χ) measured at 0.1 T using a zero-field cooling mode for 4*H*-$BaMnO_3$ single crystals. The inset shows the derivative of susceptibility. (b) Temperatrue dependence of specific heat (C_p) measured below 300 K at zero field. The inset shows the fitting result (black curve) for specific heat below 15 K as described in the text. (c) Field-dependent isothermal magnetization (M) curves measured at selected temperatures with the field perpendicular to the (001) plane for 4*H*-$BaMnO_3$ single crystals. (d) Magnetization measured at 200 K with the field along different crystal directions.

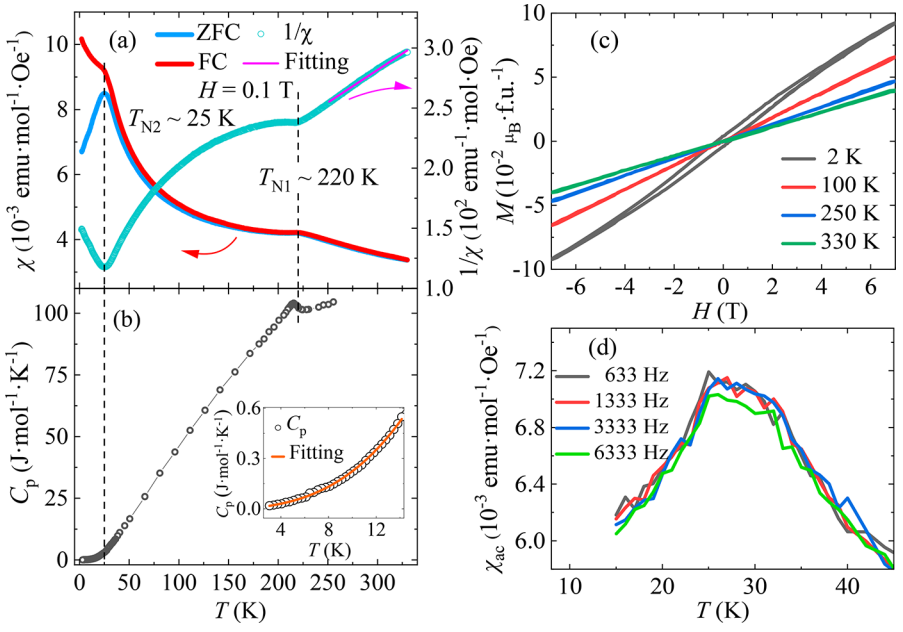

Figure 5. (a) Temperature-dependent magnetic susceptibility (χ) and inverse magnetic susceptibility ($1/\chi$) measured at 0.1 T using zero-field cooling mode for 6*H*-$BaMnO_3$. The pink line shows the Curie−Weiss fitting above 250 K. (b) Temperature dependence of specific heat (C_p) for 6*H*-$BaMnO_3$. The inset shows the fitting result (orange curve) below 15 K as described in the text. (c) Field dependence of isothermal magnetization (M) curves measured at selected temperatures. (d) Temperature dependence of ac magnetization (χ_{ac}) at different frequencies.

may have already been released well above T_{N2}. As shown in the inset of Figure 5b, the specific heat data of the 6*H* phase below 15 K can be fitted by the formula $C_p = \alpha T^{3/2} + \beta T^3$, giving $\alpha = 2.74(1) \times 10^{-3}$ J mol^{-1} K$^{-5/2}$ and $\beta = 1.37(2) \times 10^{-4}$ J mol^{-1} K^{-4}. The presence of the $T^{3/2}$ term reflects the contribution of ferromagnetic correlations as expected from the canted AFM structure below T_{N2}.

The magnetic properties of $A^{2+}Mn^{4+}O_3$ (only Mn^{4+} is a magnetic ion) perovskites are mainly related to the Mn−O−Mn bond angle in corner-sharing MnO_6 octahedra as well as

https://doi.org/10.1021/acs.inorgchem.1c02155
Inorg. Chem. 2021, 60, 16308−16315

the Mn−Mn distance in face-sharing MnO_6 octahedra. According to the Goodenough−Kanamori−Anderson rules,[38,39] the Mn^{4+}−O−Mn^{4+} superexchange interaction with a bond angle close to 180° in corner-sharing MnO_6 octahedra favors the strong AFM ordering. In addition to the corner-sharing MnO_6 octahedra, there also exist face-sharing octahedral dimers in $BaMnO_3$, giving rise to the Mn^{4+}−Mn^{4+} direct exchange interaction due to the moderate overlapping of Mn 3d orbitals.[40] The symbol of the direct exchange integral is related to the Mn−Mn distance. A shorter Mn−Mn distance is favorable for AFM ordering.[41] $CaMnO_3$ crystallizes into a $GdFeO_3$-type structure with space group *Pnma*, where the MnO_6 octahedra are all corner-sharing, with the average Mn−O−Mn bond angle being about 157.8°.[12] The compound forms G-type AFM ordering at 125 K.[12,16] In comparison with $CaMnO_3$, the Mn^{4+}−O−Mn^{4+} bond angle of the corner-sharing MnO_6 octahedra increases to 177.8° in the 6*H*-$BaMnO_3$ and 180.0° in the 4*H* phase. As a result, the AFM-phase transition temperatures increase to 220 K in the former and 263 K in the later. In the 4*H* phase, two face-sharing MnO_6 octahedra form a dimer (i.e., a Mn_2O_9 unit) along the *c*-axis direction. The Mn^{4+}−Mn^{4+} direct interaction causes some 1D AFM short-range corrections at temperatures above T_N.[16,21] In the 6*H* phase, however, the corner-sharing Mn_2O_9 units are separated from each other by MnO_6 octahedral layers in the *ab* plane. Consequently, the spin-chain-like structure is broken, and the 6*H* phase does not show the 1D AFM feature. Instead, a second long-range AFM ordering takes place at a lower temperature of T_{N2}. This AFM ordering most probably arises from the *ab*-plane spin interaction. The exact origin remains to be determined in the future. Anyway, it is the different structural constitutions that lead to distinct magnetic properties between the 4*H*- and 6*H*-type $BaMnO_3$.

CONCLUSIONS

For the first time, we prepared a stoichiometric 4*H*-$BaMnO_3$ single crystal as well as its polymorphic 6*H* phase by using the floating zone method combined with high-pressure techniques. Both phases crystallize into hexagonal perovskite structures with the same $P6_3/mmc$ space group, but they exhibit different MnO_6 octahedral connections and stacks. Specifically, two face-sharing MnO_6 octahedra form Mn_2O_9 dimers, which align 1D-like chains by sharing the corner O atoms along the *c*-axis direction in the 4*H* phase. In the 6*H* phase, however, the corner-sharing Mn_2O_9 dimers are separated from each other by MnO_6 octahedral layers in the *ab* plane, breaking the chain structure of the dimers. As a result, some short-range 1D AFM correlations are found to occur in the 4*H* phase but are absent in the 6*H* phase. In addition, a single long-range AFM phase transition is observed in the 4*H* phase at $T_N \approx 263$ K. In comparison, two AFM transitions show up in the 6*H* phase at $T_{N1} \approx 220$ K and $T_{N2} \approx 25$ K, respectively. The reduced AFM ordering temperature with the structural variation from 4*H* to 6*H* can be attributed to the decreased Mn−O−Mn bond angle, while the 6*H*-phase AFM transition occurring at T_{N2} may arise from the spin interaction between the MnO_6 octahedra in the *ab* plane. This work provides a desirable material system for studying structure-determined distinct magnetic properties.

ASSOCIATED CONTENT

Supporting Information

The Supporting Information is available free of charge at https://pubs.acs.org/doi/10.1021/acs.inorgchem.1c02155.

Some information about the crystal structure of 4*H*-$BaMnO_{2.73}$, including the XRD pattern and Rietveld refinement results; refined structure parameters (PDF)

Accession Codes

CCDC 2109406 and 2109407 contain the supplementary crystallographic data for this paper. These data can be obtained free of charge via www.ccdc.cam.ac.uk/data_request/cif, or by emailing data_request@ccdc.cam.ac.uk, or by contacting The Cambridge Crystallographic Data Centre, 12 Union Road, Cambridge CB2 1EZ, UK; fax: + 44 1223 336033.

AUTHOR INFORMATION

Corresponding Author

Youwen Long − *Beijing National Laboratory for Condensed Matter Physics, Institute of Physics, Chinese Academy of Sciences, Beijing 100190, China; School of Physical Sciences, University of Chinese Academy of Sciences, Beijing 100049, China; Songshan Lake Materials Laboratory, Dongguan, Guangdong 523808, China;* orcid.org/0000-0002-8587-7818; Email: ywlong@iphy.ac.cn

Authors

Shijun Qin − *Beijing National Laboratory for Condensed Matter Physics, Institute of Physics, Chinese Academy of Sciences, Beijing 100190, China; School of Physical Sciences, University of Chinese Academy of Sciences, Beijing 100049, China*

Yi-Ying Chin − *Department of Physics, National Chung Cheng University, Chiayi 62102, Taiwan;* orcid.org/0000-0003-2316-0747

Bowen Zhou − *Beijing National Laboratory for Condensed Matter Physics, Institute of Physics, Chinese Academy of Sciences, Beijing 100190, China; School of Physical Sciences, University of Chinese Academy of Sciences, Beijing 100049, China*

Zhehong Liu − *Beijing National Laboratory for Condensed Matter Physics, Institute of Physics, Chinese Academy of Sciences, Beijing 100190, China; School of Physical Sciences, University of Chinese Academy of Sciences, Beijing 100049, China*

Xubin Ye − *Beijing National Laboratory for Condensed Matter Physics, Institute of Physics, Chinese Academy of Sciences, Beijing 100190, China; School of Physical Sciences, University of Chinese Academy of Sciences, Beijing 100049, China*

Jia Guo − *Beijing National Laboratory for Condensed Matter Physics, Institute of Physics, Chinese Academy of Sciences, Beijing 100190, China; School of Physical Sciences, University of Chinese Academy of Sciences, Beijing 100049, China*

Guangxiu Liu − *Beijing National Laboratory for Condensed Matter Physics, Institute of Physics, Chinese Academy of Sciences, Beijing 100190, China; School of Physical Sciences, University of Chinese Academy of Sciences, Beijing 100049, China*

Chien-Te Chen − *National Synchrotron Radiation Research Center, Hsinchu 30076, Taiwan*

Zhiwei Hu − *Max Planck Institute for Chemical Physics of Solids, Dresden 01187, Germany*

Complete contact information is available at: https://pubs.acs.org/10.1021/acs.inorgchem.1c02155

Notes

The authors declare no competing financial interest.

■ ACKNOWLEDGMENTS

This work was supported by the National Natural Science Foundation of China (grant nos. 11934017, 51772324, and 11921004), the National Key R&D Program of China (grant nos. 2018YFE0103200 and 2018YFA0305700), the Beijing Natural Science Foundation (grant no. Z200007), and the Chinese Academy of Sciences (grant nos. XDB33000000 and QYZDBSSW-SLH013). We acknowledge support from the Max Planck-POSTECH-Hsinchu Center for Complex Phase Materials.

■ REFERENCES

(1) Pickett, W. E.; Singh, D. J. Electronic Structure and Half-Metallic Transport in the $La_{1-x}Ca_xMnO_3$ System. *Phys. Rev. B: Condens. Matter Mater. Phys.* **1996**, *53* (3), 1146−1160.

(2) Liu, Z.; Sakai, Y.; Yang, J.; Li, W.; Liu, Y.; Ye, X.; Qin, S.; Chen, J.; Agrestini, S.; Chen, K.; Liao, S. C.; Haw, S. C.; Baudelet, F.; Ishii, H.; Nishikubo, T.; Ishizaki, H.; Yamamoto, T.; Pan, Z.; Fukuda, M.; Ohashi, K.; Matsuno, K.; Machida, A.; Watanuki, T.; Kawaguchi, S. I.; Arevalo-Lopez, A. M.; Jin, C.; Hu, Z.; Attfield, J. P.; Azuma, M.; Long, Y. Sequential Spin State Transition and Intermetallic Charge Transfer in $PbCoO_3$. *J. Am. Chem. Soc.* **2020**, *142* (12), 5731−5741.

(3) Abbas, S. K.; Aslam, M. A.; Amir, M.; Atiq, S.; Ahmed, Z.; Siddiqi, S. A.; Naseem, S. Electrical Impedance Functionality and Spin Orientation Transformation of Nanostructured Sr-Substituted $BaMnO_3$ Hexagonal Perovskites. *J. Alloys Compd.* **2017**, *712*, 720−731.

(4) Zhou, J. S.; Goodenough, J. B. Unusual Evolution of the Magnetic Interactions Versus Structural Distortions in $RMnO_3$ Perovskites. *Phys. Rev. Lett.* **2006**, *96* (24), 247202.

(5) Ribeiro, J. L. Coexistence of Orbital and CE-AFM Orders in Colossal Magnetoresistance Manganites: A Symmetry Perspective. *Phys. B* **2016**, *492*, 55−60.

(6) Torregrosa-Rivero, V.; Albaladejo-Fuentes, V.; Sánchez-Adsuar, M.-S.; Illán-Gómez, M.-J. Copper Doped $BaMnO_3$ Perovskite Catalysts for NO Oxidation and NO_2-Assisted Diesel Soot Removal. *RSC Adv.* **2017**, *7* (56), 35228−35238.

(7) Wang, X.; Chai, Y.; Zhou, L.; Cao, H.; Cruz, C. D.; Yang, J.; Dai, J.; Yin, Y.; Yuan, Z.; Zhang, S.; Yu, R.; Azuma, M.; Shimakawa, Y.; Zhang, H.; Dong, S.; Sun, Y.; Jin, C.; Long, Y. Observation of Magnetoelectric Multiferroicity in a Cubic Perovskite System: $LaMn_3Cr_4O_{12}$. *Phys. Rev. Lett.* **2015**, *115*, 087601.

(8) Zhou, B.; Qin, S.; Ma, T.; Ye, X.; Guo, J.; Yu, X.; Lin, H. J.; Chen, C. T.; Hu, Z.; Tjeng, L. H.; Zhou, G.; Dong, C.; Long, Y. High-Pressure Synthesis of Two Polymorphic $HgMnO_3$ Phases and Distinct Magnetism from 2D to 3D. *Inorg. Chem.* **2020**, *59* (6), 3887−3893.

(9) Søndenå, R.; Stølen, S.; Ravindran, P.; Grande, T.; Allan, N. L. Corner- Versus Face-Sharing Octahedra in $AMnO_3$ Perovskites (A = Ca, Sr, and Ba). *Phys. Rev. B: Condens. Matter Mater. Phys.* **2007**, *75* (18), 184105.

(10) Goldschmidt, V. M. The Laws of Crystal Chemistry. *Naturwissenschaften* **1926**, *14*, 477−485.

(11) Adkin, J. J.; Hayward, M. A. $BaMnO_{3-x}$ Revisited: A Structural and Magnetic Study. *Chem. Mater.* **2007**, *19* (4), 755−762.

(12) Paszkowicz, W.; Piętosa, J.; Woodley, S. M.; Dłużewski, P. A.; Kozłowski, M.; Martin, C. Lattice Parameters and Orthorhombic Distortion of $CaMnO_3$. *Powder Diffr.* **2010**, *25* (1), 46−59.

(13) Battle, P. D.; Gibb, T. C.; Jones, C. W. The Structural and Magnetic Properties of $SrMnO_3$: A Reinvestigation. *J. Solid State Chem.* **1988**, *74*, 60−66.

(14) Syono, Y.; Akimoto, S.-i.; Kohn, K. Structure Relations of Hexagonal Perovskite-Like Compounds ABX_3 at High Pressure. *J. Phys. Soc. Jpn.* **1969**, *26* (4), 993−999.

(15) Nielsen, M. B.; Ceresoli, D.; Parisiades, P.; Prakapenka, V. B.; Yu, T.; Wang, Y.; Bremholm, M. Phase Stability of the $SrMnO_3$ Hexagonal Perovskite System at High Pressure and Temperature. *Phys. Rev. B: Condens. Matter Mater. Phys.* **2014**, *90* (21), 214101.

(16) Belik, A. A.; Matsushita, Y.; Katsuya, Y.; Tanaka, M.; Kolodiazhnyi, T.; Isobe, M.; Takayama-Muromachi, E. Crystal Structure and Magnetic Properties of *6H*-$SrMnO_3$. *Phys. Rev. B: Condens. Matter Mater. Phys.* **2011**, *84* (9), 094438.

(17) Satapathy, S.; Singh, M. K.; Pandit, P.; Gupta, P. K. Relaxor Ferroelectric Behavior of $BaMnO_3$ (2*H*) at Room Temperature. *Appl. Phys. Lett.* **2012**, *100* (4), 042904.

(18) Cussen, E. J.; Battle, P. D. Crystal and Magnetic Structures of 2*H* $BaMnO_3$. *Chem. Mater.* **2000**, *12* (3), 831−838.

(19) Chamberland, B. L.; Sleight, A. W.; Weiher, J. F. Preparation and Characterization of $BaMnO_3$ and $SrMnO_3$ Polytypes. *J. Solid State Chem.* **1970**, *1*, 506−511.

(20) Boullay, Ph.; Hervieu, M.; Labbe, Ph.; Raveau, B. Single Crystal and HREM Study of the "Bi-Sr" Stabilized $BaMnO_3$ 9*R* Polytype. *Mater. Res. Bull.* **1997**, *32* (1), 35−42.

(21) Adkin, J. J.; Hayward, M. A. Structure and Magnetism of 4H-BaMnO3−x ($0 \le x \le 0.35$) and 4H-Ba0.5Sr0.5MnO3−x ($0 \le x \le 0.21$). *J. Solid State Chem.* **2006**, *179* (1), 70−76.

(22) Parras, M.; Alonso, J.; Gonzalez-Calbet, J.M.; Vallet-Regı, M. Ordering and Defects in $BaMnO_{3-y}$ ($0.22 \le y \le 0.40$). *J. Solid State Chem.* **1995**, *117*, 21−29.

(23) Long, Y.; Kaneko, Y.; Ishiwata, S.; Taguchi, Y.; Tokura, Y. Synthesis of Cubic $SrCoO_3$ Single Crystal and Its Anisotropic Magnetic and Transport Properties. *J. Phys.: Condens. Matter* **2011**, *23* (24), 245601.

(24) Long, Y. W.; Kaneko, Y.; Ishiwata, S.; Tokunaga, Y.; Matsuda, T.; Wadati, H.; Tanaka, Y.; Shin, S.; Tokura, Y.; Taguchi, Y. Evolution of Magnetic Phases in Single Crystals of $SrFe_{1-x}Co_xO_3$ Solid Solution. *Phys. Rev. B: Condens. Matter Mater. Phys.* **2012**, *86* (6), 064436.

(25) Liu, Y.; Liu, Z.; Li, Z.; Qin, S.; Ye, X.; Shen, X.; Zhou, B.; Zhou, G.; Agrestini, S.; Valvidares, M.; Vasili, H. B.; Hu, Z.; Long, Y. Multiple Magnetic Transitions and Electrical Transport Transformation of a $BaFeO_3$ Cubic Perovskite Single Crystal. *Phys. Rev. B: Condens. Matter Mater. Phys.* **2020**, *101* (14), 144421.

(26) Larson, A. C.; Von Dreele, R. B. *General Structure Analysis System (GSAS)*; Report No. LAUR 86-748; Los Alamos National Laboratory: Los Alamos, NM, 1994.

(27) Arévalo-López, A. M.; Attfield, J. P. High-Pressure $BaCrO_3$ Polytypes and the 5*H*-$BaCrO_{2.8}$ Phase. *J. Solid State Chem.* **2015**, *232*, 236−240.

(28) Pellegrin, E.; Tjeng, L. H.; de Groot, F. M. F.; Hesper, R.; Sawatzky, G. A.; Moritomo, Y.; Tokura, Y. Soft X-ray Magnetic Circular Dichroism Study of the Colossal Magnetoresistance Compound $La_{1-x}Sr_xMnO_3$. *J. Electron Spectrosc. Relat. Phenom.* **1997**, *86*, 115−118.

(29) Mitra, C.; Hu, Z.; Raychaudhuri, P.; Wirth, S.; Csiszar, S. I.; Hsieh, H. H.; Lin, H. J.; Chen, C. T.; Tjeng, L. H. Direct Observation of Electron Doping in La0.7Ce0.3MnO3 Using X-ray Absorption Spectroscopy. *Phys. Rev. B: Condens. Matter Mater. Phys.* **2003**, *67* (9), 092404.

(30) Vasiliev, A. N.; Volkova, O. S.; Lobanovskii, L. S.; Troyanchuk, I. O.; Hu, Z.; Tjeng, L. H.; Khomskii, D. I.; Lin, H. J.; Chen, C. T.; Tristan, N.; Kretzschmar, F.; Klingeler, R.; Büchner, B. Valence States and Metamagnetic Phase Transition in Partially B-site-disordered Perovskite $EuMn_{0.5}Co_{0.5}O_3$. *Phys. Rev. B: Condens. Matter Mater. Phys.* **2008**, *77* (10), 104442.

(31) Burnus, T.; Hu, Z.; Hsieh, H. H.; Joly, V. L. J.; Joy, P. A.; Haverkort, M. W.; Wu, H.; Tanaka, A.; Lin, H.-J.; Chen, C. T.; Tjeng, L. H. Local Electronic Structure and Magnetic Properties of

$LaMn_{0.5}Co_{0.5}O_3$ Studied by X-ray Absorption and Magnetic Circular Dichroism Spectroscopy. *Phys. Rev. B: Condens. Matter Mater. Phys.* **2008**, *77* (12), 125124.
(32) Liu, H.; Zhou, J.; Zhang, L.; Hu, Z.; Kuo, C.; Li, J.; Wang, Y.; Tjeng, L. H.; Pi, T.-W.; Tanaka, A.; Song, L.; Wang, J.-Q.; Zhang, S. Insight into the Role of Metal−Oxygen Bond and O 2p Hole in High-Voltage Cathode $LiNi_xMn_{2-x}O_4$. *J. Phys. Chem. C* **2017**, *121* (30), 16079−16087.
(33) Wu, H.; Burnus, T.; Hu, Z.; Martin, C.; Maignan, A.; Cezar, J. C.; Tanaka, A.; Brookes, N. B.; Khomskii, D. I.; Tjeng, L. H. Ising Magnetism and Ferroelectricity in Ca_3CoMnO_6. *Phys. Rev. Lett.* **2009**, *102* (2), 026404.
(34) Hollmann, N.; Hu, Z.; Willers, T.; Bohatý, L.; Becker, P.; Tanaka, A.; Hsieh, H. H.; Lin, H. J.; Chen, C. T.; Tjeng, L. H. Local Symmetry and Magnetic Anisotropy in Multiferroic $MnWO_4$ and Antiferromagnetic $CoWO_4$ Studied by Soft X-ray Absorption Spectroscopy. *Phys. Rev. B: Condens. Matter Mater. Phys.* **2010**, *82* (18), 184429.
(35) Simonson, J. W.; Yin, Z. P.; Pezzoli, M.; Guo, J.; Liu, J.; Post, K.; Efimenko, A.; Hollmann, N.; Hu, Z.; Lin, H. J.; Chen, C. T.; Marques, C.; Leyva, V.; Smith, G.; Lynn, J. W.; Sun, L. L.; Kotliar, G.; Basov, D. N.; Tjeng, L. H.; Aronson, M. C. From Antiferromagnetic Insulator to Correlated Metal in Pressurized and Doped LaMnPO. *Proc. Natl. Acad. Sci. U. S. A.* **2012**, *109* (27), E1815−9.
(36) Guo, J.; Shen, X.; Liu, Z.; Qin, S.; Wang, W.; Ye, X.; Liu, G.; Yu, R.; Lin, H. J.; Chen, C. T.; Tjeng, L. H.; Hu, Z.; Long, Y. High-Pressure Synthesis of a B-site Co^{2+}/Mn^{4+} Disordered Quadruple Perovskite $LaMn_3Co_2Mn_2O_{12}$. *Inorg. Chem.* **2020**, *59* (17), 12445−12452.
(37) Woodfield, B. F.; Wilson, M. L.; Byers, J. M. Low-Temperature Specific Heat of $La_{1-x}Sr_xMnO_{3-\delta}$. *Phys. Rev. Lett.* **1997**, *78* (16), 3201−3204.
(38) Goodenough, J. B. Theory of the Role of Covalence in the Perovskite-Type Manganites [La, M(II)]MnO_3. *Phys. Rev.* **1955**, *100* (2), 564−573.
(39) Kanamori, J. Superexchange Interaction and Symmetry Properties of Electron Orbitals. *J. Phys. Chem. Solids* **1959**, *10* (2−3), 87−98.
(40) Daoud-Aladine, A.; Martin, C.; Chapon, L. C.; Hervieu, M.; Knight, K. S.; Brunelli, M.; Radaelli, P. G. Structural Phase Transition and Magnetism in Hexagonal $SrMnO_3$ by Magnetization Measurements and by Electron, X-ray, and Neutron Diffraction Studies. *Phys. Rev. B: Condens. Matter Mater. Phys.* **2007**, *75* (10), 104417.
(41) Marasinghe, G. K.; Han, J.; James, W. J.; Yelon, W. B.; Ali, N. The Relationship Between Magnetic Interactions and Near Neighbor Interatomic Distances in the Transition Metal Sublattice of $R(Mn/Fe)_6A_6$ (R = Nd or Sm, A = Ge or Sn). *J. Appl. Phys.* **2002**, *91* (10), 7863−7865.
(42) Shannon, R. D. Revised Effective Ionic Radii and Systematic Studies of Interatomie Distances. *Acta Crystallogr., Sect. A: Cryst. Phys., Diffr., Theor. Gen. Crystallogr.* **1976**, *32*, 751−767.
(43) Brown, I. D.; Altermatt, D. Bond-Valence Parameters Obtained from a Systematic Analysis of the Inorganic Crystal Structure Database. *Acta Crystallogr., Sect. B: Struct. Sci.* **1985**, *41*, 244−247.

https://doi.org/10.1021/acs.inorgchem.1c02155
Inorg. Chem. 2021, 60, 16308−16315